Central European Journal of Energetic Materials
ISSN 1733-7178; e-ISSN 2353-1843

Cent. Eur. J. Energ. Mater. 2019, *16*(4): 564-582; DOI 10.22211/cejem/115262
Article is available in PDF-format, in colour, at:
http://www.wydawnictwa.ipo.waw.pl/cejem/Vol-16-Number-4-2019/CEJEM_00982.pdf

Research paper

Interior Perforation Flow Field Study of Partially Cut 7-Perforated Stick Propellants

Xiaoliang Zhao, Xiaobing Zhang*

Nanjing University of Science and Technology, China
**E-mail:* zhangxb680504@163.com

Abstract: Partially cut 7-perforated propellants are used in gun charges because of their good flame spreading, high progressivity and loading density. To investigate the complex flow field in a partially cut multi-perforation stick propellant, a steady three-dimensional model for compressible viscid internal perforation and the vent gas region flow field was established and simulated by ANSYS Fluent. The results illustrate that the cut vent can decrease the internal perforation pressure and end face gas velocity. Moreover, the mass that escaped through the vent to the outside was 85.3% of the whole internal burning propellant gas. When the width of the cut slot was larger than half the diameter, the internal pressure decreased weakly and the progressive intensity decreased slightly as the cut slot was increased. As the same side intervals were increased or the perforation diameters were decreased, the end face gas velocity and the internal and external perforation pressure differences increased, and the propellant combustion area progressive intensity increased. As the web thickness increased, the internal pressure increased, and gas velocity exhibited an upward tendency and reached peak values when $2e_1 = 0.84$ mm, whilst the progressive intensity increased slightly.

Keywords: partially cut, 7-perforation stick propellants, internal perforation flow field, pressure difference, gas velocity

1 Introduction

Long stick propellant charges offers many advantages over conventional multi-perforation granular propellants in large caliber gun systems [1-4]. The flow resistance of stick propellant is lower than that of a random grain charge, thus flame spreading is faster and more reproducible. Zhang *et al.* [5-7] constructed a stick propellant interior ballistic model in order to study the interior ballistics process; the erosive burning and pressure difference can be clearly affected by the propellant length, the internal perforation diameter and the loading density, especially during the initial period. Although overly long stick propellant may lead to propellant rupture and cause severe erosive burning, the burning surface of slotted single perforation stick propellant is not a progressive combustion process.

The U.S. Army Research Laboratory developed a partially cut multi-perforation stick propellant charge system [8]. This multi-perforated stick propellant charge is attractive for both its progressivity and loading density. The ballistic performance can be improved by an optimized web and the muzzle velocity can be increased by 6% both in actual gun firing and in ballistics calculation results. The partially cut multi-perforation stick propellant segments separate, tumble, and behave like a traditional granular propellant [9, 10], as the interior ballistics cycle proceeds. Recently, Xiao *et al.* [11, 12] studied the influence of the cutting parameters on the gas generation rate using a closed bomb and tested the internal perforation diameter distribution through an interrupted bomb with different venting parameters. The results showed that proper venting parameters can reduce the erosive burning effect of a multi-perforated stick propellant. Xiao *et al.* [13] also calculated the burnt mass fraction and the burning surface area of 7-perforation partially cut propellant grains using the level set method; the propellant combustion process obeys Piobert's law, and the combustion area is just like grain propellant with the same diameter dimensions. However, the specific internal perforation flow fields within the propellant appear to be unavailable for experimental measurement because the propellant combustion is uninterruptible and the small size of the propellant also increases the complexity of any experiments. As such, an investigation of the internal perforation flow field could provide a more comprehensive study of internal perforation pressure and gas velocity distribution.

In the present work, an internal perforation flow field mathematical model was established and numerical simulations were carried out in the framework of ANSYS Fluent, in order to analyze the flow field of partially cut 7-perforation

internal perforation propellant that is not easily achieved by current experimental techniques. The purpose of this work was to study the internal perforation fluid flow conditions with different venting parameters to obtain a better understanding of the complex internal flow process.

2 Physical Model

The flow field of the total propellant gas regions consists of two parts: the internal perforation region and the cut-off venting gas region. The total internal propellant surfaces are both the 7 internal perforations and the cut vent surfaces. In this paper, a steady flow field was studied; propellant deformations and fracture were ignored, and the burned propellant gas release on the propellant surface ignored the chemical reaction process. The internal perforation propellant gas escapes both at the propellant end face perforation and the cut vent space. The 7-perforation partially cut propellant parameters, such as the minimum interval between the cut slots on the same side, the minimum interval between the cut slots on the reverse side and the cut slot width, are shown as Figure 1.

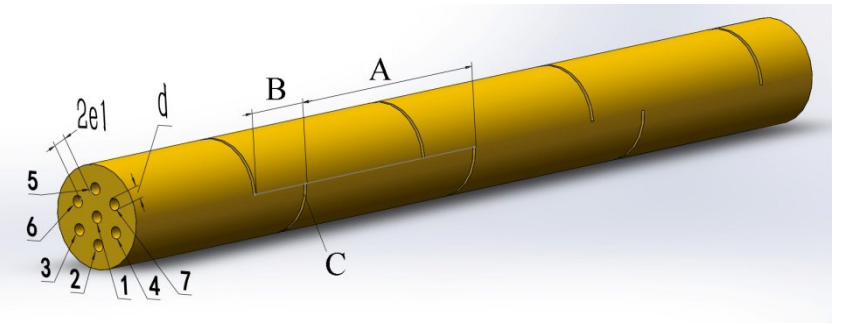

Figure 1. Schematic of venting method of 7-perforation stick propellant: A – the same side interval, B – the reverse side interval, C – the cut slot width, $2e_1$ – propellant web thickness, d – internal perforation diameter; 1, 2, 3, 4, 5, 6 and 7 – perforation number

3 Mathematical Model

The governing equations couple the standard Navies-Stoke equations with the turbulence equations and the transport equations as follows [14]. The $k-\varepsilon$ turbulence model is employed with two equations of turbulence kinetic energy and dissipation. The coupled equations can be written in a uniform

vector form:

$$\frac{\partial \boldsymbol{Q}}{\partial t}+\frac{\partial \boldsymbol{E}_i}{\partial x_i}+\frac{\partial \boldsymbol{V}_i}{\partial x_i}=\boldsymbol{H} \tag{1}$$

where $\boldsymbol{Q}=\begin{pmatrix}\rho\\ \rho u_j\\ e\\ \rho k\\ \rho\varepsilon\end{pmatrix}$ $\boldsymbol{E}_i=\begin{pmatrix}\rho u_i\\ \left(\rho u_i u_j+p_t\right)\delta_{ij}\\ \left(e+p_t\right)u_j\\ \rho u_i k\\ \rho u_i \varepsilon\end{pmatrix}$ $\boldsymbol{V}_i=\begin{pmatrix}0\\ \tau_{ij}\\ u_j\tau_{ij}+\lambda\dfrac{\partial T}{\partial x_i}\\ \mu_k\dfrac{\partial k}{\partial x_i}\\ \mu_\varepsilon\dfrac{\partial \varepsilon}{\partial x_i}\end{pmatrix}$

The standard $k-\varepsilon$ turbulence model is as follows:

The Reynolds stresses $\overline{u_i' u_j'}$ are related to the shear stress of the flow (τ_{ij}) by the following equation:

$$\tau_{ij}=-\rho\overline{u_i' u_j'} \tag{2}$$

where ρ is the density of the fluid, and we define τ_{ij} as follows:

$$\tau_{ij}=-\mu_t\left(\frac{\partial \bar{u}_i}{\partial x_j}+\frac{\partial \bar{u}_j}{\partial x_i}\right)-\frac{2}{3}\rho k\delta_{ij} \tag{3}$$

where μ_t is the turbulent viscosity. In the standard $k-\varepsilon$ turbulence model, the turbulent viscosity is defined as:

$$\mu_t=\rho C_\mu\frac{k^2}{\varepsilon} \tag{4}$$

where C_μ is the model constant. $\sigma_k = 1.0$, $\sigma_\varepsilon = 1.3$, $C_{\varepsilon 1} = 1.44$, $C_{\varepsilon 2} = 1.92$ and $C_\mu = 0.09$ are all empirical model constants

4 Numerical Approaches and Boundary Conditions

There are three boundary conditions for the symmetry of the propellant internal flow field model, which are shown as in Figure 2. The mid-surfaces are set to the symmetry surfaces. The internal perforation end faces and the cut vent surfaces are taken as the pressure out boundary, and the steady pressure is set. The mass burning rate and injection total temperature are set to the propellant burning surface. Normal injection of the propellant gas is enforced by employing the no-slip boundary condition. Erosive burning effects are ignored, and the mass injection flux is defined as follows [14]:

$$m_{flux} = \rho_p \cdot \dot{r} \tag{5}$$

$$\dot{r} = ap^n \tag{6}$$

where ρ_p is the propellant density; $\dot{r}$ is the propellant burning rate; p is the local propellant surface pressure; a is the propellant burning coefficient; and n is the pressure index. The gas properties were taken from [15] and the boundary conditions are summarized in Table 1.

Table 1. Correlative parameters of the propellant gas

Parameter	$2e_1$ [mm]	d [mm]	A [mm]	B [mm]	C [mm]	Pressure out [MPa]
Value	0.840	0.30	20	3	0.15	10
Parameter	k [W·(m·k)$^{-1}$]	μ [kg·(m·k)$^{-1}$]	C_p [J·(kg·K)$^{-1}$]	M [kg·kmol^{-1}]	T_f [K]	m_{flux} [kg·m^{-2}·s^{-1}]
Value	0.2083	$8.25 \cdot 10^{-5}$	2020	25	3000	10

The correctness of the results depends greatly on the resolution of the grid, a higher grid resolution will give better result accuracy. The 3-D geometry is discretized using a hexahedral mesh by ICEM software. A structured mesh is used in the internal perforation and vent gas region, respectively. The combined mesh technique is employed, and the connected faces are set as the interfacial face. The mesh near the propellant surface and the vent hole is refined locally as shown in Figure 2. The local mesh refinement approach is used near the propellant surface, the internal perforation and the vent turning regions; the total number of cells was 33940000.

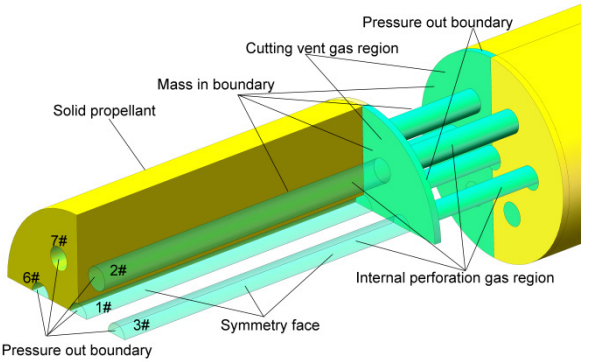

(a)

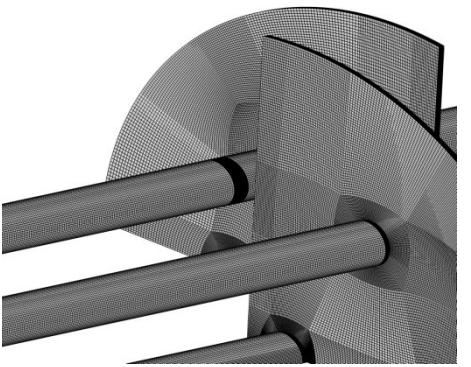

(b)

Figure 2. Boundary conditions and mesh of the propellant gas flow region: (a) the internal perforation calculation region and boundary conditions, (b) the mesh near the propellant surface and the vent hole

A SIMPLE algorithm for pressure-velocity coupling with a second-order upwind discretization scheme was used to obtain the solution for the equations of momentum, turbulence kinetic energy, and turbulence dissipation rate. The convergence residuals of the continuity, velocity, and the turbulence parameters were set to be 10^{-3}. At the same time the mass flow rate difference of the mass-in and pressure-out boundary was monitored. Steady calculation results are considered to have been achieved when the mass flow rate difference is less than 10^{-8}, and the convergence residual is less than 10^{-3}, respectively.

5 Results and Discussion

The pressure distributions of the internal perforation and cut vent gas region are shown in Figure 3. The maximum pressure value was 11.9 MPa, located at 50 mm in 7# perforation, the maximum gas velocity was 271.0 $m \cdot s^{-1}$ at the end face. In the 43 mm cut vent region, the maximum pressure of the cut region was 11.0 MPa, which is located at the 1# perforation centre point. The pressure decreased gradually as the location is closed to the pressure-out surface.

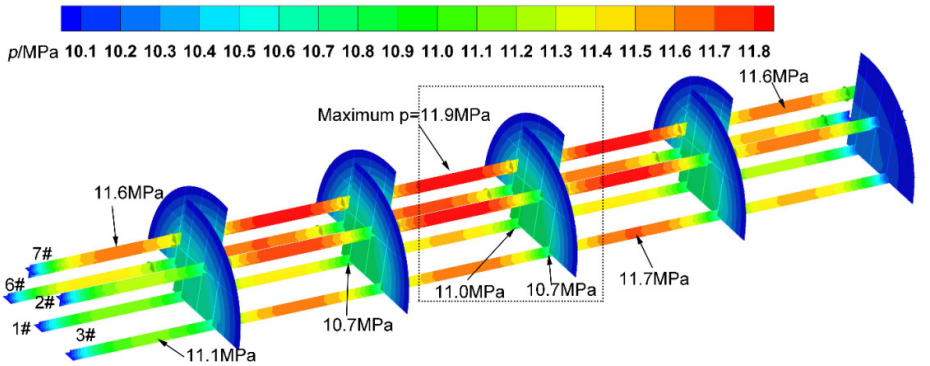

Figure 3. Internal flow field pressure distribution

The local streamline distributions of the internal perforation and the 43 mm cut vent region are shown in Figure 4. The maximum velocity was 271.0 $m \cdot s^{-1}$ located at 80 mm from the end face in 7# perforation. The streamlines of the 43 mm cut vent region show the gas flow path, the 2# and 3# internal perforations gas flow out directly to the external. The centre 1# perforation outflow gas flows out in both channels: one is the space between the 2# and 3# perforations, and the other is between 2# and the cut surface.

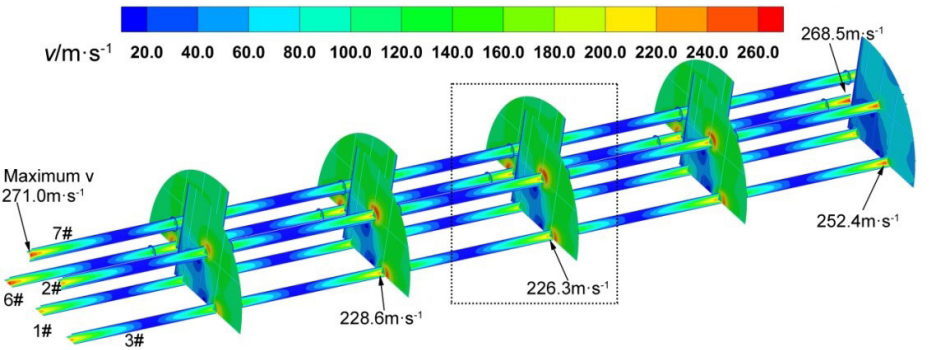

(a)

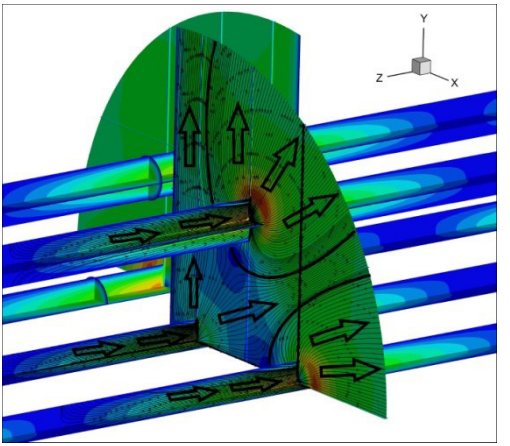

(b)

Figure 4. Internal flow field velocity distribution and the local streamline: (a) velocity distribution in the internal flow field, (b) 43 mm cut vent streamline

The different perforation pressure and velocity distributions in the axial direction are shown in Figure 5. Compared with the different perforation maximum pressures, the 2# and 7# perforation maximum pressures were about 11.9 MPa in the largest level. The 3# and 6# perforation maximum pressures were about 11.7 MPa in the second level. The 1# perforation maximum pressure was the smallest because the 1# perforation propellant gas can escape through both sides of the cut vent, *i.e.* the 1# internal perforation's largest length was 17 mm compared with the other perforation lengths of 20 mm, the length

to diameter was the smallest. All perforation gas velocities at all of the different location vent faces, such as 20, 23, 40, 43, 60, 63, 80 and 83 mm vents, were about 225 m·s^{-1} in the 2#, 3#, 6# and 7# perforations; the 1# perforation gas velocity at the cut vent was the smallest at about 190 m·s^{-1}.

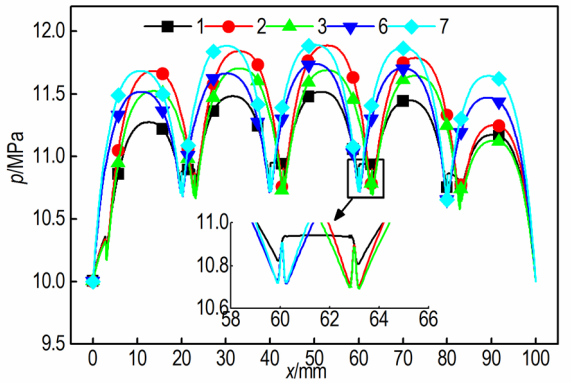

(a)

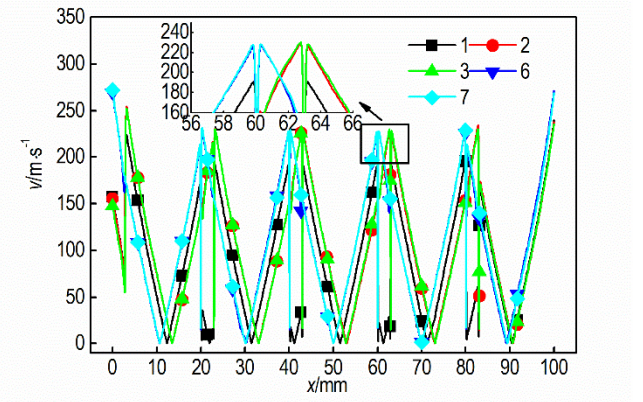

(b)

Figure 5. Pressure (a) and velocity (b) distribution of partially cut propellant in the axial direction

5.1 Influence of width of cut slot on pressure and velocity

The 6# perforation pressure distributions for different cut slot widths are shown in Figure 6. The 6# perforation pressure decreased with increasing cut slot width. The maximum pressure occurred at 50 mm and the 50 mm peak

pressure was larger than the 30 and 70 mm pressures when the cut slot width was less than 0.125 mm. When the cut slot width was larger than 0.150 mm, the five pressures, such as at 10, 30, 50, 70, and 90 mm, were nearly the same, *i.e.* the internal perforation flow character at each interval were nearly same.

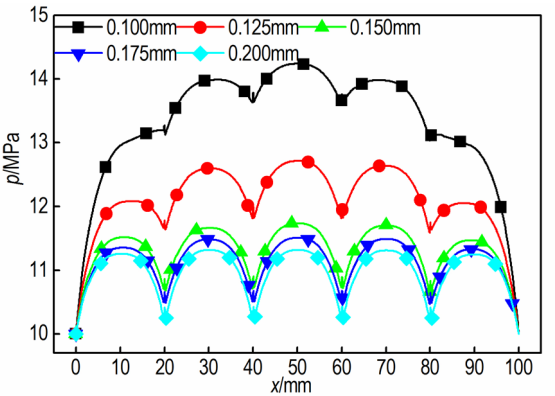

Figure 6. The 6# perforation pressure distribution for different cut slot widths

The 6# perforation maximum pressure and 60 mm vent gas velocity for different cut slot widths are shown in Figure 7. The maximum pressure decreased and the 60 mm vent gas velocity increased with increasing of cut slot width. When the cut slot width was larger than 0.150 mm, the maximum pressure was less than 11.75 MPa, *i.e.* the pressure difference was less than 1.75 MPa, and the 60 mm vent gas velocity was about 230 $m \cdot s^{-1}$.

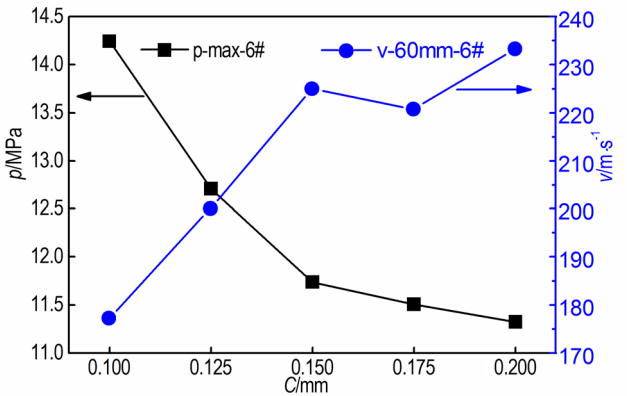

Figure 7. The 6# perforation maximum pressure and 60 mm vent gas velocity for different cut slot widths

The propellant combustion gas generation rate was affected by the propellant geometry and size. For a 7-perforation propellant, the propellant grain is progressive, *i.e.* the combustion surface area increases as burning proceeds. The progressive intensity is described by the dimensionaless parameter σ, which is defined as the ratio of the propellant surface area (S_Z) to the initial propellant surface area ($S_{initial}$), as follows:

$$\sigma = \frac{S_Z}{S_{initial}} \tag{7}$$

The progressive properties of different cut slot widths are shown in Figure 8, where Z is the relative burning thickness, which is defined as the ratio of the burned propellant thickness to half of the web thickness. The progressive intensity decreased as the cut slot width was increased, but the influence was very weak.

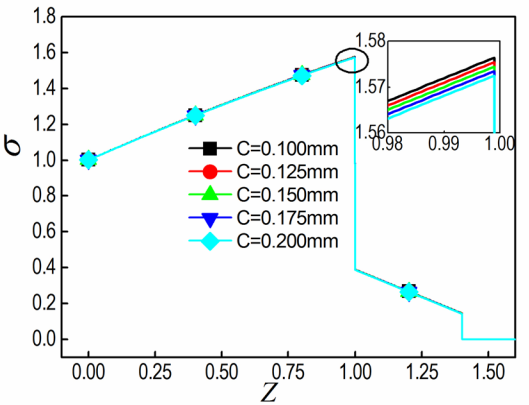

Figure 8. The progressive property for different cut slot widths

5.2 Influence of same side interval on pressure and velocity

The 6# perforation maximum pressure and 60 mm vent gas velocity for different same side intervals are shown in Figure 9. The maximum pressure and 60 mm vent gas velocity obviously increase with an increase in the same side interval. The maximum pressure for a 24 mm same side interval was 12.25 MPa, with a pressure difference of 2.25 MPa. The overly large pressure difference could lead to propellant rupture in a large same side interval. The progressive property for same side intervals are shown in Figure 10. The progressive intensity increased as the same side interval was increased from 8 to 24 mm.

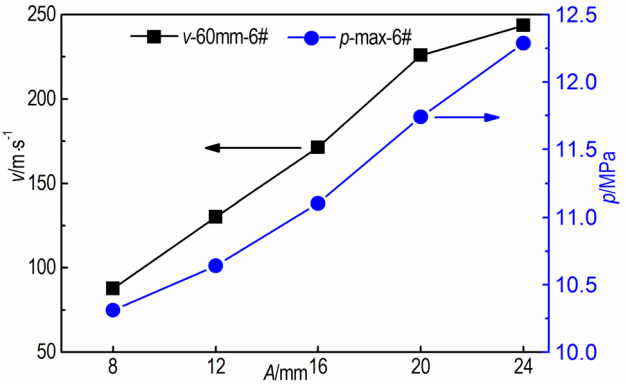

Figure 9. The 6# perforation maximum pressure and 60 mm vent gas velocity for different same side intervals

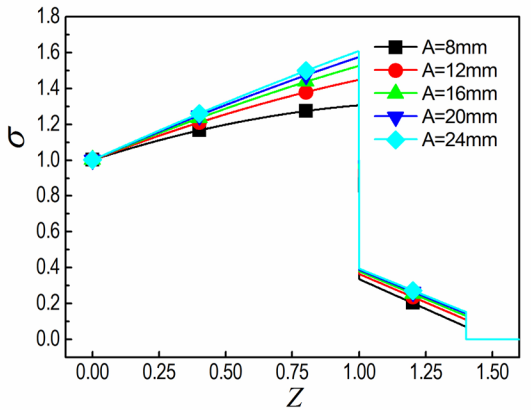

Figure 10. The progressive property for different same side intervals

5.3 Influence of reverse side interval on pressure and velocity

The 6# perforation pressure distribution for different reverse side intervals is shown in Figure 11. The 6# perforation pressure in a 3 mm reverse side interval reached the maximum value. 6# perforation maximum pressure and 60 mm vent gas velocity for different reverse side intervals are shown in Figure 12. The maximum pressure occurred when the reverse side intervals were 3 mm. The maximum pressure was 11.7 MPa and the minimum was 11.3 MPa, the difference being 0.4 MPa. The maximum velocity was 227 $m \cdot s^{-1}$ and the minimum was 207 $m \cdot s^{-1}$, the velocity difference being 10 $m \cdot s^{-1}$. Compared with the influence of other parameters, the reverse side interval

has a very weak influence on the pressure and gas velocity, and the reverse side interval has no influence on the propellant progressive property.

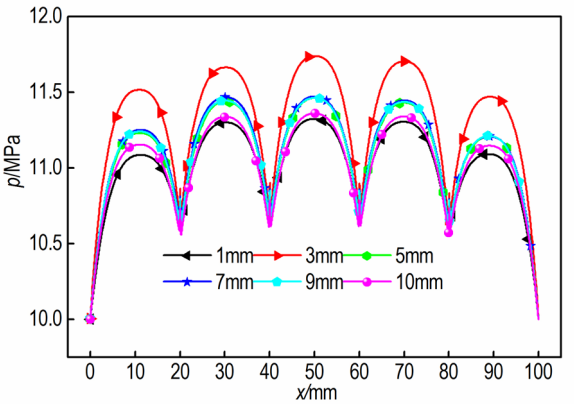

Figure 11. The 6# perforation pressure distribution for different reverse side intervals

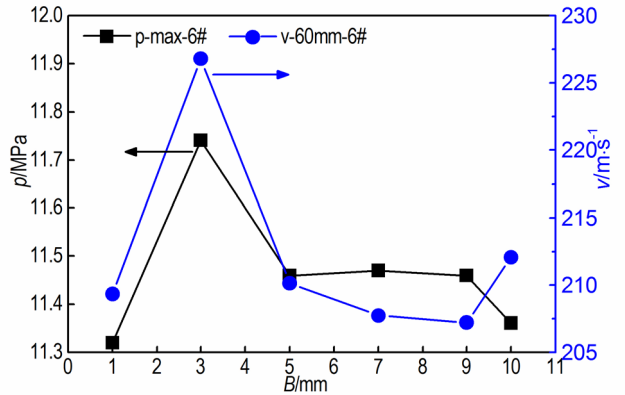

Figure 12. The 6# perforation maximum pressure and 60 mm vent gas velocity for different reverse side intervals

5.4 Influence of internal perforation diameter on pressure and velocity

The 6# perforation pressure distribution for different internal perforation diameters is shown in Figure 13. The internal perforation maximum pressure increased with a decrease in internal perforation diameter, the d = 0.2 mm maximum pressure was much larger than in the cases of 0.3 mm and 0.4 mm.

The ratio of length to diameter is the critical factor, the propellant gas resistance escapes through the end face and the vent region is large when the length to diameter ratio is large. The cut slot width is a constant 0.15 mm, but the vent region pressure increased with an increase in diameter, the internal perforation propellant surface of large diameter is larger, resulting in a larger propellant gas mass flux and vent pressure.

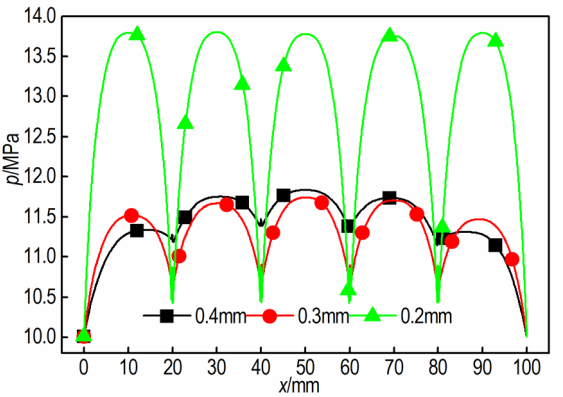

Figure 13. The 6# perforation pressure distribution for different internal perforation diameters

The 6# perforation maximum pressure and 60mm vent gas velocity for different perforation diameters are shown in Figure 14. Both the 6# perforation maximum pressure and 60 mm vent gas velocity decreased with an increase in the internal perforation diameter. The maximum pressure was 13.8 MPa with $d = 0.2$ mm, and the pressure decreased to 11.8 MPa as the diameter was increased to 0.4 mm. The 60 mm vent gas velocity decreased from 348.5 to 156.7 $m \cdot s^{-1}$. The progressive property for different perforation diameters is shown in Figure 15. The progressive intensity increased as the perforation diameter was decreased from 0.4 to 0.2 mm.

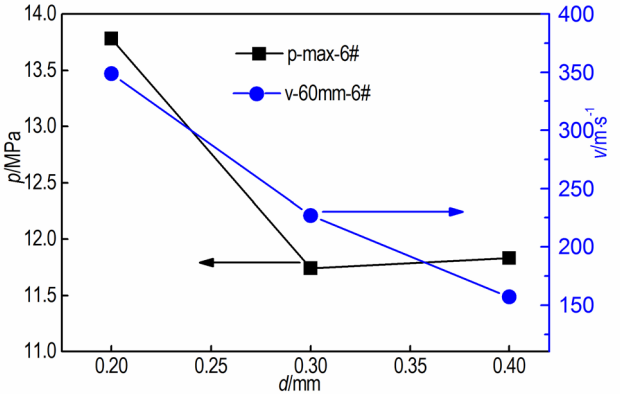

Figure 14. The 6# perforation maximum pressure and 60 mm vent gas velocity for different internal perforation diameters

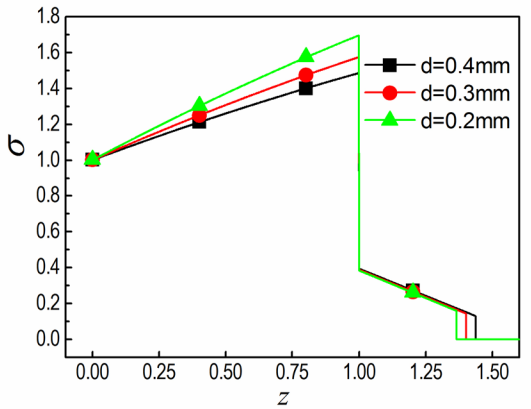

Figure 15. The progressive property for different internal diameters

5.5 Influence of web thickness on pressure and velocity

Large outer diameters have resistance, which is decided by the internal perforation diameter and the web thickness. The 6# perforation pressure distributions for different web thicknesses are shown in Figure 16. The internal perforation pressure increased with an increase in web thickness. The internal perforation propellant gas has a larger resistance in the partially cut slot region with the web thickness $2e_1$ = 1.092 mm, which resulted in the large pressure.

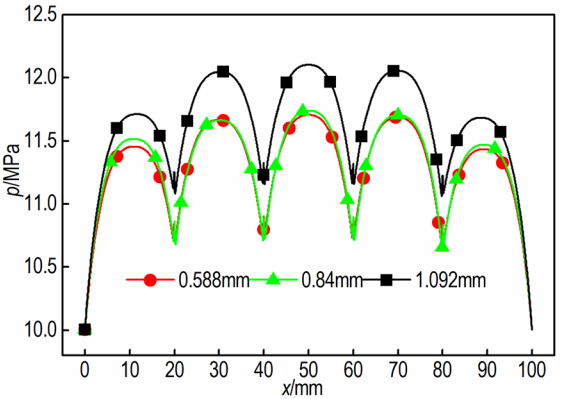

Figure 16. The 6# perforation pressure distribution for different web thicknesses

The 6# perforation maximum pressure and 60 mm vent gas velocity for different web thicknesses are shown in Figure 17. When the web thickness was increased from 0.588 to 1.092 mm, the maximum pressure increased from 11.77 to 12.1 MPa. At the same time the 60 mm vent gas velocity increased accordingly, the maximum and minimum velocities were 226.8 and 217.8 $m \cdot s^{-1}$, respectively, the velocity difference being 9.0 $m \cdot s^{-1}$. The progressive property for different web thicknesses is shown in Figure 18. The progressive intensity increased slightly as the web thickness was increased from 0.588 to 1.092 mm.

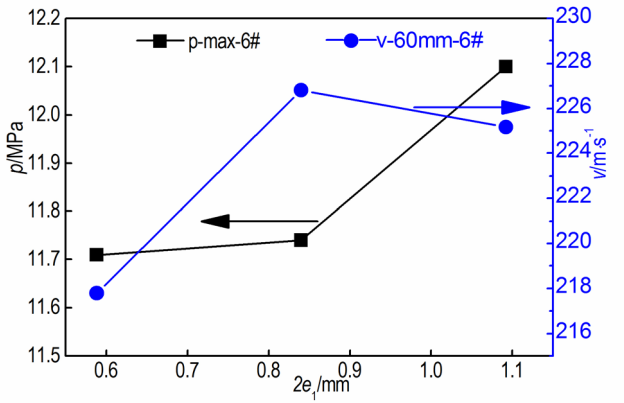

Figure 17. The 6# perforation maximum pressure and 60 mm vent gas velocity for different web thicknesses

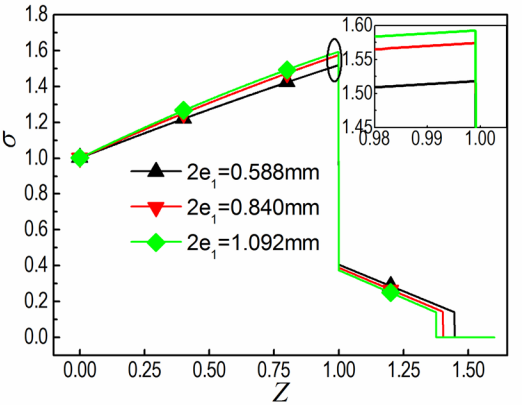

Figure 18. The progressive property for different web thicknesses

6 Conclusions

In this paper, a model for the internal perforation gas region of partially cut 7-perforation stick propellant and the cut slot region was established and carried out by ANSYS Fluent. The simulation results showed that the partial cutting technique can mitigate the internal perforation pressure and the end face gas velocity. The internal perforation maximum pressure decreased as the cut slot width was increased; the internal gas can escape through the vent with little resistance when the cut width is larger than half the internal diameter. The length to diameter ratio is a vital parameter in influencing the pressure and gas velocity and the propellant combustion area progressive intensity. Larger same side intervals or smaller internal parameters make the length to diameter ratio larger, causing the internal perforation pressure, gas velocity and the propellant combustion area progressive intensity to increase, while the reverse side intervals have only a weak influence. Larger web thicknesses result in propellant out diameter and larger resistance, so the internal perforation pressure is increased and the cut vent gas velocity becomes less. The progressive intensity increased very weakly as the web thickness was increased.

References

[1] Char, J.M.; Kuo, K.K. Study of Combustion Processes of Single-Perforated Stick Propellants. *J. Propul. Power* **1989**, *5*: 262-268.

[2] Hsieh, W.H.; Kuo, K.K. *A Study of Flame Spreading and Combustion Phenomena of Stick Propellants.* Pennsylvania State University Park Report, PA, USA, **1988**.

[3] Hsieh, W.H.; Char, J.M.; Zanotti, C.; Kuo, K.K. Erosive and Strand Burning of Stick Propellants. Part I. Measurements of Burning Rates and Thermal-wave Structures. *J. Propul. Power* **1990**, *6*: 392-399.

[4] Hsieh, W.H.; Kuo, K.K. Erosive and Strand Burning of Stick Propellants. Part II. Theoretical Modeling of Erosive-burning Processes. *J. Propul. Power* **1990**, *6*: 400-406.

[5] Zhao, X.; Zhang, X. Study of Stick-propellant Gun Interior Ballistic Considering Internal Perforation Erosive Burning. *Int. Symp. Ballistics, Proc., 29th,* Edinburgh, UK, **2016**, 880-887.

[6] Zhao, X.; Zhang, X. Investigation of Stick Propellant Internal Perforation Erosive Burning on Interior Ballistics Performances. *Def. Sci. J.* **2017**, *67*: 19-25.

[7] Rashad, M.; Zhang, X.; Elsadek, H. Interior Ballistic Two-phase Flow Model of Guided-projectile Gun System Utilizing Stick Propellant Charge. *WSEAS Trans. Appl. Theor. Mech.* **2014**, *9*: 124-135.

[8] Routh, R.; Robbins, F.W.; Koszoru, A.A. *A New High-Progressivity/High-Density Propulsion Concept: Partially Cut Multiperforated Stick Propellant.* U.S. Army Ballistic Research Lab., Aberdeen Proving Ground Report BRL-TR-3189, USA, **1991**.

[9] Routh, C.R; Horst, A.W. *Detailed Characterization of Hypervelocity Firings in a Long 120-mm Gun.* U.S. Army Ballistic Research Lab., Aberdeen Proving Ground Report BRL-TR-3190, USA, **1991**.

[10] Routh, C.R.; Robbins, F.W.; Horst, A.W. *Experimental Hypervelocity Firings Using Stick and Granular Propellant Configurations.* U.S. Army Ballistic Research Lab., Aberdeen Proving Ground, Report BRL-TR-3921, USA, **1991**.

[11] Xu, H.T.; Xiao, Z.; He, W.D. Combustion Characteristics of Partially Cut Multiperforated Stick Propellant. (in Chinese) *Chin. J. Energ. Mater*. (*Hanneng Cailiao)* **2014**, *22*(2): 251-255.

[12] Xiao, Z.; Xu, H.; He, W. Influence of Venting Parameters on Erosive Burning of Partially Cut Multi-perforated Stick Propellants. *Sci.* Tech. Energ*etic Materials* **2015**, *76*(1): 42-46.

[13] Xiao, Z.; He, W.; Xu, H. Emulation and Calculation of the Burning Surface of 3D Grains of Partially Cut Multi-perforated Stick Propellant Using the Level Set Method. *Propellants Explos. Pyrotech.* **2016**, *41*: 148-153.

[14] Venkateswaran, S.; Deshpande, M.; Merkle, C.L. The Application of Preconditioning to Reacting Flow Computations. *AIAA CFD Conf., 12th,* San Diego, CA, AIAA 95-1673, **1995**, 306-316.

[15] Willcox, M.A.; Brewster, M.Q.; Tang, K.C.; Stewart, D.S.; Kuznetsov, I. Solid

Rocket Motor Internal Ballistics Simulation Using Three-Dimensional Grain Burnback. *J. Propul. Power* **2007**, *3*, 575-584.

[16] Summerfield, M.; Price, E.W; De Luca, L. *Nonsteady Burning and Combustion Stability of Solid Propellants.* AIAA, Washington, DC, **1992**, pp. 717-779; ISBN 978-1-56347-014-1.

Received: September 25, 2018
Revised: December 12, 2019
First published online: December 19, 2019